

High-efficiency acceleration of an electron beam in a plasma wakefield accelerator

M. Litos¹, E. Adli^{1,2}, W. An³, C. I. Clarke¹, C. E. Clayton⁴, S. Corde¹, J. P. Delahaye¹, R. J. England¹, A. S. Fisher¹, J. Frederico¹, S. Gessner¹, S. Z. Green¹, M. J. Hogan¹, C. Joshi⁴, W. Lu⁵, K. A. Marsh⁴, W. B. Mori³, P. Muggli⁶, N. Vafaei-Najafabadi⁴, D. Walz¹, G. White¹, Z. Wu¹, V. Yakimenko¹ & G. Yocky¹

High-efficiency acceleration of charged particle beams at high gradients of energy gain per unit length is necessary to achieve an affordable and compact high-energy collider. The plasma wakefield accelerator is one concept^{1–3} being developed for this purpose. In plasma wakefield acceleration, a charge-density wake with high accelerating fields is driven by the passage of an ultra-relativistic bunch of charged particles (the drive bunch) through a plasma^{4–6}. If a second bunch of relativistic electrons (the trailing bunch) with sufficient charge follows in the wake of the drive bunch at an appropriate distance, it can be efficiently accelerated to high energy. Previous experiments using just a single 42-gigaelectronvolt drive bunch have accelerated electrons with a continuous energy spectrum and a maximum energy of up to 85 gigaelectronvolts from the tail of the same bunch in less than a metre of plasma⁷. However, the total charge of these accelerated electrons was insufficient to extract a substantial amount of energy from the wake. Here we report high-efficiency acceleration of a discrete trailing bunch of electrons that contains sufficient charge to extract a substantial amount of energy from the high-gradient, nonlinear plasma wakefield accelerator. Specifically, we show the acceleration of about 74 picocoulombs of charge contained in the core of the trailing bunch in an accelerating gradient of about 4.4 gigavolts per metre. These core particles gain about 1.6 gigaelectronvolts of energy per particle, with a final energy spread as low as 0.7 per cent (2.0 per cent on average), and an energy-transfer efficiency from the wake to the bunch that can exceed 30 per cent (17.7 per cent on average). This acceleration of a distinct bunch of electrons containing a substantial charge and having a small energy spread with both a high accelerating gradient and a high energy-transfer efficiency represents a milestone in the development of plasma wakefield acceleration into a compact and affordable accelerator technology.

The experiment reported here is carried out in the three-dimensional, nonlinear regime of plasma wakefield acceleration, also known as the blow-out regime⁸. In this regime, a tightly focused and short ultra-relativistic electron bunch with a density greater than the plasma density propagates through a long column of plasma. $\sigma_r \lesssim c/\omega_p$ and $\sigma_z \lesssim \pi c/\omega_p$ are the root-mean-square (r.m.s.) transverse and longitudinal sizes of the beam, respectively, with ω_p the plasma frequency. The transverse electric field of this drive bunch expels all of the plasma electrons within a radius of about 30 μm , as shown in the three-dimensional particle-in-cell (QuickPIC^{9,10}) simulation depicted in Fig. 1a. The Coulomb field of the stationary ions pulls the expelled plasma electrons back towards the central axis, which begins the wake oscillation, producing periodic ion cavities in the plasma. This wake structure follows the beam trajectory with a phase velocity matched to the drive bunch, at nearly the speed of light.

In the simulation, the input plasma and beam parameters are similar to those measured in the experiment with a simple scaling of the total beam charge (see Methods). The on-axis longitudinal electric field E_z of

the wake, also depicted in Fig. 1a, shows that the bulk of the drive bunch is located in a region of positive (forward-directed) electric field, and thus loses energy. If the electrons in the rear of such a drive bunch were to extend into the negative region of the electric field, they would gain energy from the wake. If there were not enough charge in the long tail of electrons to have a non-negligible impact on the profile of the steep

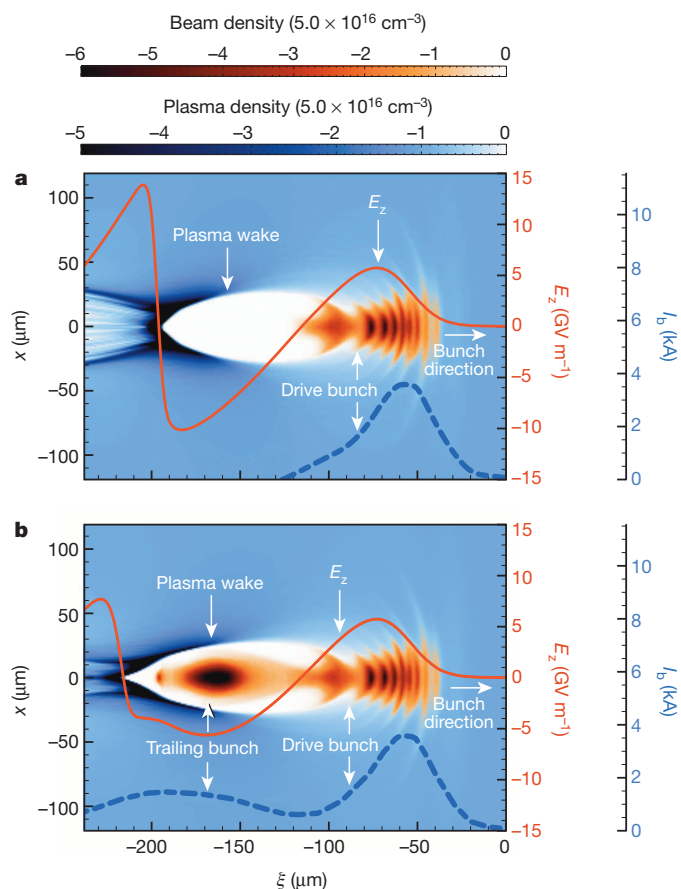


Figure 1 | Three-dimensional particle-in-cell simulation of beam-driven plasma wakefield interaction. **a**, A slice through the centre of an unloaded plasma wake, where x is the dimension transverse to the motion, and $\xi = z - ct$ is the dimension parallel to the motion, E_z is the on-axis longitudinal electric field (red solid line) and I_b is the current of the input beam (blue dotted line). **b**, A plasma wake generated by the same drive bunch as in **a** when loaded by a trailing bunch. The plasma electron density is represented in blue, while the beam density is represented in red. The ion density (not shown) is uniform. The particle-in-cell code QuickPIC^{9,10} was used to generate this simulation of the beam-plasma interaction.

¹SLAC National Accelerator Laboratory, Menlo Park, California 94025, USA. ²Department of Physics, University of Oslo, 0316 Oslo, Norway. ³Department of Physics and Astronomy, University of California Los Angeles, Los Angeles, California 90095, USA. ⁴Department of Electrical Engineering, University of California Los Angeles, Los Angeles, California 90095, USA. ⁵Department of Engineering Physics, Tsinghua University, Beijing 100084, China. ⁶Max Planck Institute for Physics, Munich 80805, Germany.

wakefield E_z , they would end up with a large final energy spread and leave behind a substantial amount of unused energy in the wake, as was the case in earlier experiments^{11–13}.

The key to achieving a high energy-transfer efficiency with a narrow final energy spread is in placing an appropriately shaped trailing bunch at precisely the correct distance behind the drive bunch so as to flatten the wakefield E_z and provide for a uniform energy gain throughout the trailing bunch^{14,15}. Theory and simulations have shown that a trailing bunch with a Gaussian distribution and the right charge content can lead to a nearly flattened wakefield^{8,15}. Figure 1b shows an approximately double-Gaussian (in z) input-charge distribution for both the drive and trailing bunches. The wakefield is noticeably altered by the addition of the trailing bunch charge, that is, the beam has loaded the wake. Note that the initial extent of the trailing bunch extends past the first ion cavity period (the region void of electrons), or ‘bucket’ of the wake. This leads to loss of charge because some of the electrons in the trailing bunch are strongly defocused by the returning plasma electrons at the back of the first bucket.

To reach accelerating gradients on the scale of more than a gigaelectronvolt per metre, the plasma medium must have a high electron density, which results in a correspondingly short plasma wavelength. This necessitates a very small separation between the drive and trailing bunches, and such a configuration is non-trivial to produce with ultra-relativistic electron beams¹⁶. The typical scale of a plasma wakefield acceleration wake structure at a plasma density of $5 \times 10^{16} \text{ cm}^{-3}$ is around 200 μm , as can be seen in Fig. 1, and therefore the separation between the charge-density peaks of the two bunches must be less than this value. The Facility for Advanced Accelerator Experimental Tests (FACET) at the SLAC National Accelerator Laboratory, where the experiment was carried out, was designed specifically to produce such high-current drive and trailing bunches with an appropriately small separation.

In the experiment, the SLAC linear accelerator provides a 20.35-GeV electron beam to the FACET experimental area, where it is then manipulated to form a two-bunch structure (see Methods) just before entering the plasma source, which is a 36-cm-long, laser-ionized column of lithium vapour with a density of $5 \times 10^{16} \text{ cm}^{-3}$ contained inside a heat pipe oven^{17,18} (see Methods). The final charge delivered to the plasma totals 1.80 nC, with 1.02 nC contained in the drive bunch ($\sigma_z = 25 \mu\text{m}$, $I_{\text{peak}} = 4.9 \text{ kA}$), and 780 pC contained in the broader trailing bunch ($\sigma_z = 47 \mu\text{m}$, $I_{\text{peak}} = 2.0 \text{ kA}$). Not all of this charge is coupled into the plasma wake, however, owing to the oversized width and length of the trailing bunch. After exiting the plasma, the spectrum of the electrons was diagnosed using a two-screen imaging magnetic spectrometer (see Methods).

Figure 2 shows examples of electron spectra from three individual electron beam shots. The first shot, shown in Fig. 2a, gives the nominal spectrum of the two-bunch beam when the plasma source is not present. The second shot, shown in Fig. 2b, shows the measured spectrum when the plasma source is present and the spectrometer is set to optimally image 20.35-GeV electrons. This setting allows the energy loss of the drive bunch to be well characterized, while the trailing bunch, which has gained energy and has a higher divergence than the decelerated drive bunch, is strongly defocused. Of the approximately 1 nC of charge contained in the drive bunch entering the plasma, approximately $450 \text{ pC} \pm 63 \text{ pC}$ ($\pm \text{s.d.}$) appears at energies lower than 20.35 GeV. Figure 2c shows the spectrum of another shot similar to that shown in Fig. 2b but with the spectrometer set to image 22.35 GeV. Because the mean energy of the accelerated trailing bunch is close to the energy focus, it can readily be seen on the detector, whereas now the lowest-energy portion of the drive bunch has been strongly defocused, as expected. The centroid of the trailing bunch core in this shot has gained about 1.6 GeV of energy. The charge contained in the core of the accelerated portion of the spectrum is determined by an asymmetric Gaussian fit to the peak of the spectral projection for each shot (see Methods). The result of the core fit for the shot in Fig. 2c is shown in Fig. 2d as the dashed red line. Of the approximately 800 pC in the initial trailing bunch, the simulation indicates that only

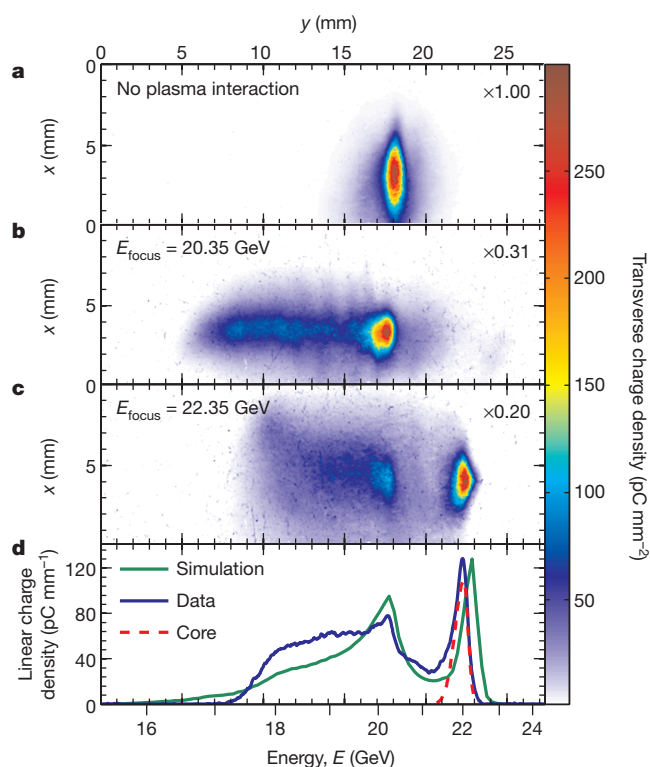


Figure 2 | Energetically dispersed beam profiles. **a**, The dispersed electron beam profile without plasma interaction, where the spectrometer is set to image 22.35 GeV. Because the beam divergence is small, the entire spectrum of the beam is well resolved even at this imaging set point. **b** and **c**, The dispersed beam profile after the electron bunches have interacted with the plasma, where the spectrometer is set to image 20.35 GeV and 22.35 GeV, respectively: E_{focus} in **b** and **c**. The left x and top y axes correspond to the actual scale of the electron beam recorded at the spectrometer diagnostic screen, while the bottom E axis shows the calibrated energy axis along the dispersive dimension y . The scaling factors in **a–c** apply to the colour scale, quantifying transverse charge density. **d**, The spatially integrated spectrum (in x) or the linear charge density of the bunches shown in **c** (solid blue line) along with the final spectrum obtained from the simulation depicted in Fig. 1b (solid green line in **d**). The core of the accelerated trailing beam is shown for the data (dashed red line).

about half of that resides in the first bucket of the wake. Of this, roughly $200 \pm 33 \text{ pC}$ of charge appears above 20.35 GeV at the detection plane with about $74 \pm 18 \text{ pC}$ of this contained in the core. The spread in charge quoted above refers to a data set containing 92 shots (discussed below). The projected energy spectrum (integrated over x) for the shot shown in Fig. 2c is presented in Fig. 2d as the blue line. For comparison, the final spectrum of the simulated two-bunch plasma wakefield acceleration interaction shown in Fig. 1b—including transport losses and the focusing effects of the imaging spectrometer set to image at 22.35 GeV—is also plotted as the green line in Fig. 2d, and shows a good qualitative agreement with the experimental spectrum.

The full data set used in this analysis consists of 92 electron beam shots taken with the imaging spectrometer set to 22.35 GeV. The projected spectral profile for each shot was obtained and the resulting 92 spectra are plotted in Fig. 3 as a waterfall plot. The profiles are sorted according to the ‘total efficiency’ of energy transfer from the drive bunch to the trailing bunch via the wake. Here, the total efficiency (shown as the black line in Fig. 3) is defined as the net energy gain of all accelerated charge in the trailing bunch divided by the net energy loss of the drive bunch (see Methods). The mean total efficiency observed in the data set is 29.1% with a standard deviation of 8.9% and a maximum value of around 50%. For comparison, the total efficiency obtained from the simulation shown in Figs 1b and 2d is 49%. The core efficiency is shown in Fig. 3 as the red

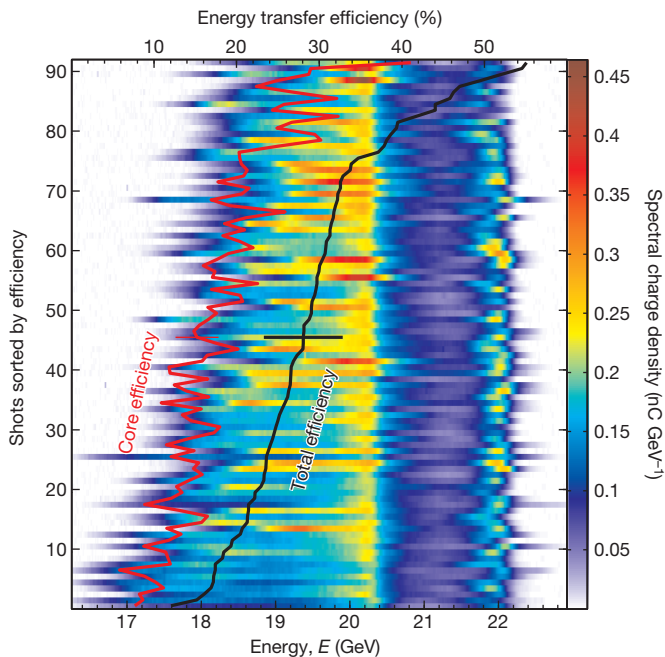


Figure 3 | Spatially integrated electron beam spectra from the data set. All 92 shots from the data set are shown with the imaging spectrometer set to image 22.35 GeV. The colour scale represents the energy spectrum in nC GeV^{-1} , similar to the blue curve of Fig. 2d, but transformed using the known dispersion of the spectrometer. The shots are sorted by the total energy-transfer efficiency (black line), as calculated using all charge above 20.35 GeV. The core energy-transfer efficiency, as calculated using only the charge found in the accelerated core of the trailing bunch, is shown as the red line. The black (or red) horizontal bar represents the typical systematic uncertainty of $\pm 5\%$ (or $\pm 3\%$) for the total energy-transfer efficiency (or core energy-transfer efficiency).

curve, which has a mean value of 17.7% with a standard deviation of 6.3%. It is lower than the total efficiency, as expected, owing to the smaller amount of charge contained in the core. The maximum core efficiency observed is over 30%.

We note that here we have measured a high energy-transfer efficiency from the drive bunch (via the wake) to the trailing bunch, though the drive bunch electrons lost only a small fraction of their total energy in our 36-cm-long plasma source. However, since the electrons in both bunches are ultra-relativistic, there is no relative motion between the bunches and the wake structure (see Fig. 1b and Supplementary Video 1), which means that the energy-transfer efficiency remains constant over the entire flat-density region of the plasma source (see Methods). Therefore, in a sufficiently long plasma source, nearly all of the energy in the drive bunch would be transferred to the trailing bunch with the same efficiency that we have measured. For the present experimental conditions, the length of the plasma would need to be extended to approximately 4 m in order to fully deplete the available energy in the drive bunch.

In this work, the average energy gain of the core of the trailing bunch is estimated to be 1.6 ± 0.1 GeV. For our plasma length of about 36-cm full-width at half-maximum (FWHM), this represents an accelerating field gradient of 4.4 GV m^{-1} , which is in good agreement with the 5 GV m^{-1} seen in the simulation (red curve in Fig. 1b). The smallest energy spread of the trailing bunch core was 0.7% (compared to the initial energy spread of the trailing bunch of about 1%; see Methods), and the average energy spread was 2.0%, where the energy spread is defined as the r.m.s. $\delta E/E$ for each shot. The simultaneous achievement of high gradient, high efficiency, and narrow energy spread demonstrated here represents an important advance in the development of a collider based on plasma wakefield acceleration¹⁹.

Increasing the peak current of the drive bunch by increasing its charge will in turn increase the amount of energy transferred from the drive

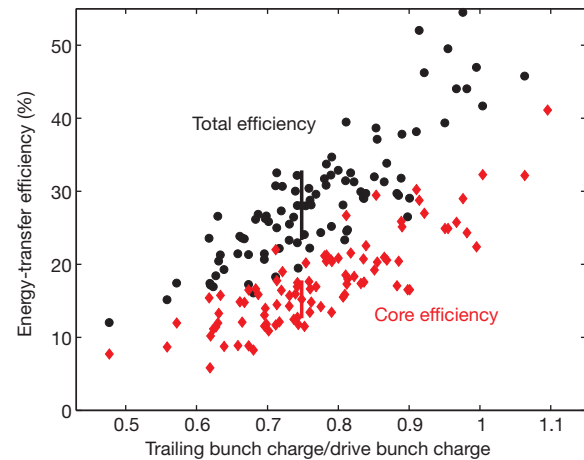


Figure 4 | Energy-transfer efficiency dependence on wake loading. The total efficiency (black circles) and core efficiency (red diamonds) versus the initial ratio of the charge in the trailing bunch to that in the drive bunch before entering the plasma source. The circles (diamonds) represent the same data that make up the black curve (red curve) in Fig. 3. The black (red) vertical bar represents the typical systematic uncertainty of $\pm 5\%$ ($\pm 3\%$) for the total energy-transfer efficiency (core energy-transfer efficiency). In this data, the total charge is held constant, and only the ratio of the charge of the trailing bunch to the charge of the drive bunch is varied.

bunch to the wake, thereby increasing the strength of the wakefield. This also increases the amount of charge needed in the trailing bunch to optimally load the wake and maximize the energy-transfer efficiency. We have used the natural spectral jitter of the incoming electron beam to measure this correlation between wake loading and energy transfer efficiency in our data.

Figure 4 shows a scatter plot of the shot-by-shot total and core efficiencies (black circles and red diamonds, respectively) obtained for the same data as in Fig. 3 plotted against the trailing-to-drive bunch charge ratio. A systematic error bar is shown for the same data point in each figure for both the total efficiency and the core efficiency values, where the leading source of uncertainty comes from the energy loss estimation (see Methods). The ratio of the charge of the trailing bunch to the charge of the drive bunch is used as a means of quantifying the loading of the wake by the trailing bunch normalized to the strength of the wake itself, which we here assume scales with the charge of the drive bunch. The observed correlation demonstrates the dependence of the energy-transfer efficiency on the loading of the wake and shows that a sufficiently high charge in the trailing bunch is necessary to attain a high efficiency. Although the final energy spread of the accelerated core of the trailing bunch is small at 2%, the increase from around 1% indicates that the shape of the trailing bunch profile inside the wake is not fully optimized for loading and flattening the wakefield, as shown in the simulation of Fig. 1b. The trailing bunch would need to be shorter in extent to more optimally flatten the wakefield.

In conclusion, high-efficiency acceleration of a distinct trailing bunch of electrons containing a substantial charge and having a small-energy spread has been demonstrated in a high-gradient, beam-driven plasma wakefield accelerator. These results bring plasma wakefield acceleration one step closer to becoming a viable accelerator technology.

Online Content Methods, along with any additional Extended Data display items and Source Data, are available in the online version of the paper; references unique to these sections appear only in the online paper.

Received 20 July; accepted 1 September 2014.

- Chen, P., Dawson, J., Huff, R. & Katsouleas, T. Acceleration of electrons by the interaction of a bunched electron beam with a plasma. *Phys. Rev. Lett.* **54**, 693–696 (1985).
- Ruth, R., Chao, A., Morton, P. & Wilson, P. A plasma wake field accelerator. *Particle Accelerators* **17**, 171–189 (1985).

3. Esarey, E., Schroeder, C. B. & Leemans, W. P. Physics of laser-driven plasma-based electron accelerators. *Rev. Mod. Phys.* **81**, 1229–1285 (2009).
4. Joshi, C. & Katsouleas, T. Plasma accelerators at the energy frontier and on tabletops. *Phys. Today* **56**, 47–53 (2003).
5. Bingham, R., Mendonca, J. & Shukla, P. Plasma based charged-particle accelerators. *Plasma Phys. Contr. Fusion* **46**, R1 (2004).
6. Caldwell, A., Lotov, K., Pukhov, A. & Simon, F. Proton-driven plasma-wakefield acceleration. *Nature Phys.* **5**, 363–367 (2009).
7. Blumenfeld, I. *et al.* Energy doubling of 42 GeV electrons in a metre-scale plasma wakefield accelerator. *Nature* **445**, 741–744 (2007).
8. Lu, W., Huang, C., Zhou, M., Mori, W. B. & Katsouleas, T. Nonlinear theory for relativistic plasma wakefields in the blowout regime. *Phys. Rev. Lett.* **96**, 165002 (2006).
9. Huang, C. *et al.* QuickPIC: a highly efficient fully parallelized PIC code for plasma-based acceleration. *J. Phys. Conf. Ser.* **46**, 190–199 (2006).
10. An, W., Decyk, V. K., Mori, W. B. & Antonsen, T. M., Jr. An improved iteration loop for the three dimensional quasi-static particle-in-cell algorithm: QuickPIC. *J. Comput. Phys.* **250**, 165–177 (2013).
11. Hogan, M. *et al.* Multi-GeV energy gain in a plasma-wakefield accelerator. *Phys. Rev. Lett.* **95**, 054802 (2005).
12. Muggli, P. *et al.* Meter-scale plasma-wakefield accelerator driven by a matched electron beam. *Phys. Rev. Lett.* **93**, 014802 (2004).
13. Barov, N. *et al.* Ultra high-gradient energy loss by a pulsed electron beam in a plasma. *IEEE Proc. (2001 Particle Accelerator Conf.)* **1**, 126–128 (2001).
14. Katsouleas, T. Physical mechanisms in the plasma wake-field accelerator. *Phys. Rev. A* **33**, 2056–2064 (1986).
15. Tzoufras, M. *et al.* Beam loading in the nonlinear regime of plasma-based acceleration. *Phys. Rev. Lett.* **101**, 145002 (2008).
16. Rosenzweig, J. B. *et al.* Experimental observation of plasma wake-field acceleration. *Phys. Rev. Lett.* **61**, 98–101 (1988).
17. Muggli, P. *et al.* Photo-ionized lithium source for plasma accelerator applications. *IEEE Trans. (Plasma Sci.)* **27**, 791–799 (1999).
18. Green, S. Z. *et al.* Laser ionized preformed plasma at FACET. *Plasma Phys. Contr. Fusion* **56**, 084011 (2014).
19. Adli, E. *et al.* A beam driven plasma-wakefield linear collider: from Higgs factory to multi-TeV. In *Electronic Proceedings of the Snowmass 2013 Community Study on the Future of High-Energy Physics* <http://arxiv.org/abs/1308.1145> (2013).

Supplementary Information is available in the online version of the paper.

Acknowledgements The FACET E200 plasma wakefield acceleration experiment was built and has been operated with funding from the United States Department of Energy. Work at SLAC was supported by DOE contract DE-AC02-76SF00515 and also through the Research Council of Norway. Work at UCLA was supported by DOE contracts DE-FG02-92-ER40727 and DE-SC0010064. Simulations were performed on the UCLA Hoffman2 and Dawson2 computers and on Blue Waters through NSF OCI-1036224. Simulation work at UCLA was supported by DOE contracts DE-SC0008491 and DE-SC0008316, and NSF contracts ACI-1339893 and PHY-0960344. The work of W.L. was partially supported by NSFC 11175102, the Thousand Young Talents Program and the Tsinghua University Initiative Scientific Research Program.

Author Contributions All authors contributed extensively to the work presented in this paper.

Author Information Reprints and permissions information is available at www.nature.com/reprints. The authors declare no competing financial interests. Readers are welcome to comment on the online version of the paper. Correspondence and requests for materials should be addressed to M.L. (litos@slac.stanford.edu).

METHODS

Generation of two-bunch beam structure. The SLAC linear accelerator provides a 20.35-GeV electron beam with a charge of 3.2 nC to the FACET experimental area. To create a two-bunch structure with a peak-to-peak separation of $\sim 135 \mu\text{m}$, a single high-charge bunch with a roughly linear head-to-tail correlated energy spread is energetically dispersed and physically segmented in a plane transverse to its direction of motion.

Extended Data Fig. 1 shows a schematic of the FACET experimental area. The five dipole bend magnets at the vertices of the 'W'-shaped beam line form a chicane, which allows for the manipulation of correlations between an electron's momentum p_z and its longitudinal position z within the bunch. In inset 1, the red-to-blue colour transition indicates the initial longitudinal energy correlation generated in the linear accelerator upstream of the experimental area. Higher energies (red) are at the head of the bunch, and there is no transverse (p_z, x) correlation at this point. After some propagation beyond the first dipole magnet in the chicane, the beam becomes highly dispersed in the transverse plane with a strong linear (p_z, x) correlation (inset 2). At this point, a 305- μm -wide, 16-mm-thick tantalum bar (the 'notching device' in Extended Data Fig. 1a), is inserted into the middle of the ~ 2 -mm-wide beam. Electrons that intercept this tantalum bar lose energy through collisions and are scattered at large angles, causing them to be ejected from the beam line by the strong magnets further downstream in the chicane. This process removes $\sim 40\%$ of the initial charge in the beam (inset 3). At a symmetric location before the final dipole of the chicane (inset 4), the (p_z, x) correlation of the bunch returns with the opposite sign. Here, a compact magnetic wiggler (Extended Data Fig. 1c) yields synchrotron X-rays that sweep across a scintillating YAG screen, creating a profile of the notched electron spectrum. This is the 'initial spectrometer', providing an optical replica of the notched electron beam spectrum. Inset 5 shows that after leaving the chicane the bunch is 'over-compressed', that is, the lower energy particles are in the front of the now segmented beam, comprising the drive bunch, while the higher energy particles are in the rear, comprising the trailing bunch. The longitudinal profile of the two-bunch structure is measured in the time domain with a transverse deflecting X-band radio-frequency structure (Extended Data Fig. 1b) that streaks the beam onto a profile monitor screen located near the plasma source.

Electron beam characteristics. The electron beam sent into the plasma source has an incoming energy of 20.35 GeV with a FWHM spread of $\pm 2\%$, and a total charge of 1.80 nC. The drive bunch contains 1.02 nC, with a r.m.s. length of $\sigma_z = 25 \mu\text{m}$, and peak current $I_{\text{peak}} = 4.9 \text{ kA}$. The broader trailing bunch contains 780 pC, with $\sigma_z = 47 \mu\text{m}$, and $I_{\text{peak}} = 2.0 \text{ kA}$. The trailing bunch also exhibits a correlated energy spread of about 1% r.m.s. The peak-to-peak separation of the two bunches is 135 μm . After exiting the chicane and before entering the plasma source, the beam is focused by a series of five quadrupole magnets, labelled the 'final focus quadrupole magnets' (Extended Data Fig. 1d), down to an r.m.s. transverse spot size of 30 μm in the middle of the plasma density up-ramp. The normalized emittance of the beam in the transverse dimensions is roughly $\epsilon_{n,x} = 358 \text{ mm mrad}$ and $\epsilon_{n,y} = 35.8 \text{ mm mrad}$. Extended Data Fig. 2 shows the longitudinal profile of a typical two-bunch beam used in the experiment, as measured by the transverse deflecting radio-frequency structure.

Plasma source. The plasma source used in this experiment is a laser-ionized column of lithium vapour contained inside a heat pipe oven^{17,18} with a uniform density of $5.0 \times 10^{16} \text{ cm}^{-3}$ over a 26-cm-long region with 10-cm density ramps on either side, giving a FWHM length of approximately 36 cm. The lithium vapour column is depicted in Extended Data Fig. 1f. Extended Data Fig. 3 shows the density profile of the neutral vapour pressure density deduced from the measured temperature profile along the oven containing the lithium as well as the simple fit used to describe the density profile in our model. The density and length of the lithium vapour is controlled through the temperature of the oven and the pressure of a room-temperature noble gas (argon) serving as a buffer for the lithium at either end of the pipe. A 200-fs-long Ti:sapphire laser pulse (Extended Data Fig. 1e) containing 250 mJ of energy is focused by a 1.5° axicon lens that produces a zero-order Bessel beam profile through the full length of the lithium vapour, which in turn creates a plasma column $\sim 1 \text{ mm}$ in diameter¹⁸. The laser arrives 100 ps before the arrival of the electron beam, which is over an order of magnitude earlier than substantial recombination of the plasma is expected to occur. Calculations indicate that the peak intensity of the laser is sufficient to ionize a ~ 20 - μm -diameter filament in the buffer gas for up to 30 cm upstream of the lithium vapour. Interaction of the beam with this filament may lead to some nonlinear focusing of the beam, preventing some of the electrons in the incoming beam from cleanly coupling into the lithium plasma and thus preventing them from participating in the experiment.

Electron imaging spectrometer. The spectrum of the electrons exiting the plasma is diagnosed with an imaging spectrometer having two diagnostic screens. An imaging quadrupole doublet, depicted in Extended Data Fig. 1g, is required to capture and deliver the electrons over the long distance between the exit of the plasma and the two screens. A strong dipole magnet, in Extended Data Fig. 1h, vertically disperses

the electrons onto the two screens, shown as Extended Data Fig. 1i. A camera viewing one screen records Cherenkov light produced by the beam in a 1.4-cm air gap between two silicon wafers, while another camera records the scintillation light produced by a phosphor screen after the electron beam has passed through it. The imaging condition at the Cherenkov screen for the analysed data shown in Figs 2c, 3 and 4 is for an energy of 22.35 GeV in both the horizontal and vertical (dispersive) plane. The imaging condition at the phosphor screen, located 1 m upstream of the Cherenkov screen, is for 22.25 GeV in the horizontal plane, and 21.50 GeV in the vertical plane. The combination of these different imaging conditions provided confidence that the signal observed in the data was not simply the result of an enhancement introduced by the focusing condition of the beam.

The spatial resolution of the spectrometer in the energy plane is dominated by scattering of the beam in the vacuum-to-air exit window. The r.m.s. multiple scattering angle due to collisions of the beam particles within the solid exit window is calculated to be 143 μrad , using standard formulae. The profile monitor is located 95 cm downstream of the exit window, yielding a contribution to the spatial resolution of 135 μm . The measured spatial resolution is about 150 μm . We define the energy resolution as the spatial resolution divided by the dispersion, times the beam energy. The dispersion induced by the spectrometer dipole, at the nominal FACET beam energy of 20.35 GeV, is 62 mm. This gives an energy resolution of 76 MeV at the nominal energy of 20.35 GeV. The energy resolution scales as energy squared, yielding an energy resolution of 91 MeV for the highest imaging energy referred to in the paper, 22.35 GeV. The total distance from the object plane to the imaging plane is 22.6 m, and the imaging properties of the spectrometer shows therefore little sensitivity to the position of the object plane on the order of 10 cm or less. For example, calculations show that the error in the imaged energy is on the order of 1% or less for particles with an angle of up to 1 mrad at the object plane and for errors of the position of the object plane up to $\pm 10 \text{ cm}$.

The beam size after the spectrometer is imaged with a magnification of 0.5 in the energetically dispersed (y) plane, and the spot size in this dimension is thus dominated by the energy spread. In the non-dispersed (x) plane, the spectrometer magnifies by a factor of 5.3, so the beam size as it appears on our diagnostic screen and as it is plotted in Fig. 2 is larger than it is at the plasma exit plane by this factor.

Plasma wakefield acceleration simulation. The simulations presented in Fig. 1 and Fig. 2d use the quasi-static, three-dimensional, particle-in-cell code QuickPIC^{9,10}. The input beam is Gaussian in both transverse and longitudinal dimensions, with r.m.s. sizes and emittance values corresponding to those measured for the experimental beam, as listed in the 'Electron beam characteristics' section. The simulated beam has zero initial energy spread and the initial charge in the simulation corresponds to roughly 75% of the charge measured upstream of the plasma source in the experiment, as this yields the best final spectrum agreement with the data in Fig. 2d. The reduced charge in the simulation is probably compensating for electrons in the experimental beam that are unable to couple into the plasma wake owing to potential factors not captured in the simulation, such as non-Gaussian tails in the charge distribution. The simulated plasma density profile was based on the measured plasma source profile: a 26-cm-long flat-top density of $5.0 \times 10^{16} \text{ cm}^{-3}$ with 10-cm-long density ramps on each side, giving a FWHM length of 36 cm.

For this simulation run, a snapshot of the particles and fields was recorded 120 times over a 51-cm propagation distance (including transition into and out of the plasma density ramps on either end), thus fully resolving the oscillations of the envelope of the electron bunch which occurs on approximately a centimetre scale. The simulation box tracks the beam-plasma interaction in the coordinates $x, y, \zeta = z - ct$; that is, the box moves at light speed, close to the velocity of the bunches, although it sees the beam and plasma in the reference frame of the laboratory. The box has a size of $601 \mu\text{m} \times 601 \mu\text{m} \times 481 \mu\text{m}$ in the two transverse dimensions and the longitudinal dimension, respectively. The number of the cells for the simulation box is $512 \times 512 \times 512$ (~ 134 million cells in total).

The full, 120-frame simulation movie from which Fig. 1b was taken is available as Supplementary Movie 1. It depicts the evolution of the two-bunch beam structure as it propagates through the plasma. The upper portion of the frame shows the charge density of the beam and the plasma wake, and the lower portion of the frame shows the evolution of the beam's energy as a function of the longitudinal position inside the plasma wake.

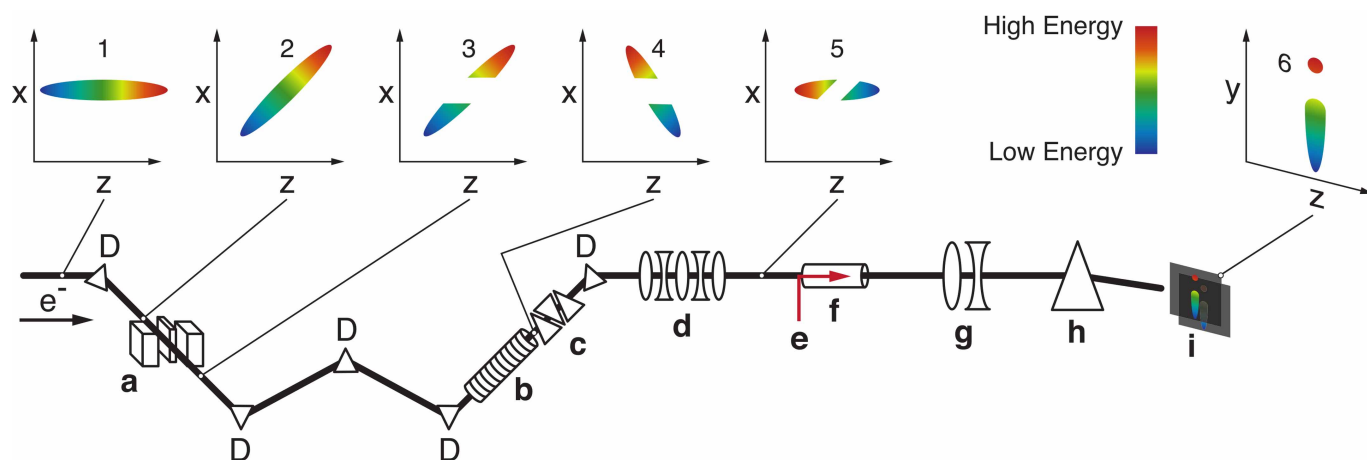
In the simulation, the drive bunch can be seen to be scalloped because the ion channel is not formed instantaneously within the beam. A slice at the front of the beam feels no focusing force while later slices feel a progressively stronger force (progressively higher betatron oscillation frequency) up to the slice that resides in the fully formed ion channel. A new scallop forms after each full betatron oscillation for the slices in the ion channel⁷. The curvature of the scalloping is due to a nonlinear dependence of the focusing force during the rise time of the bunch when the ion column is still forming. A similar scalloping structure is also observed in the experiment, as seen on the energy loss portion of the drive bunch spectrum shown in Fig. 2b.

Transfer efficiency, energy spread, and core charge estimation. The net energy gain for a particular shot is calculated as $E_{\text{gain}} = \sum_{E_i > E_0} (E_i - E_0) q_i$, where E_i is the calibrated beam energy corresponding to pixel row i on the charge-coupled device (CCD) image, $E_0 = 20.35$ GeV is the initial beam energy, and q_i is the total amount of charge observed in pixel row i . The energy loss may be calculated in the same way, though the energy loss is known to be under-represented in the 92 shots analysed in Figs 3 and 4 owing to the energy setting of the imaging quadrupoles. Thus, we instead use an estimation of the energy loss for each shot that is derived from an empirical quadratic correlation (normalized residual is 0.87) between the energy loss observed on the Cherenkov detector and the initial drive bunch charge measured upstream of the plasma source for a data set taken when the quadrupole imaging condition was set to 20.35 GeV (as in Fig. 2b) immediately before the primary 92-shot data set. For these conditions, the decelerated drive bunch could be well observed on the Cherenkov detector and the net energy loss well quantified.

To determine the energy gain of the core of the accelerated bunch, a fit was performed to the projected spectrum of each shot in the data set. Figure 2c shows a dispersed beam image of a single shot with the imaging spectrometer set to image 22.35 GeV. The spectral projection of this shot, shown in Fig. 2d, indicates a narrow peak near 22 GeV, and a more diffuse, continuous distribution of accelerated charge with a higher divergence that extends down to the initial beam energy. A fit to the projected spectrum above 21 GeV is performed that is the sum of two distinct parts: an asymmetric Gaussian to characterize the peak that occurs near 22 GeV, and a

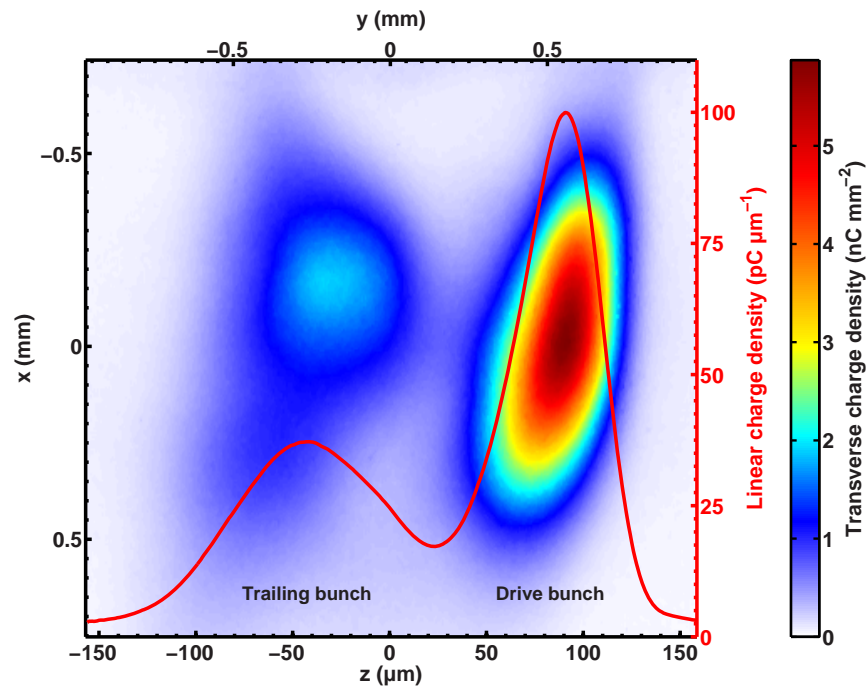
half-Gaussian to account for the diffuse, high-divergence charge. The asymmetric Gaussian portion of the fit is then used to quantify the properties of the accelerated core of the trailing bunch, such as the charge, energy gain, energy spread and energy-transfer efficiency. Extended Data Fig. 4 shows the fit that was used for the shot displayed in Fig. 2c and d, where the red line indicates the core of the accelerated trailing bunch. The same function describing the core is also shown as the dashed red line in Fig. 2d.

The 92 shots analysed in the main paper come from two data sets of 50 shots each, taken within minutes of one another, while the imaging spectrometer was set to image an energy of 22.35 GeV. Of the total 100 combined shots, 8 were rejected as outliers in which the beam-plasma interaction was substantially weaker than in the remaining 92 shots. This was quantified by the amount of ‘non-participating charge’, that is, the amount of charge found within a $\pm 2\%$ energy window about the beam’s initial energy of 20.35 GeV (corresponding to the initial beam’s FWHM energy spread), and by the energy value above the initial beam energy with the greatest charge density, or the ‘peak energy’ of the accelerated electrons. A two-dimensional cut on peak energy and non-participating charge is applied to the data that rejects the 8 low interaction shots. Five of these shots had the lowest drive-bunch charge (and thus the lowest peak current) of the complete data set. A low-peak-current drive bunch impedes the ability to form a wake in the blowout regime, leading to a weak interaction in the plasma. All eight of the rejected shots may also have had large transverse sizes, which can similarly impede the ability to form a strong wake.



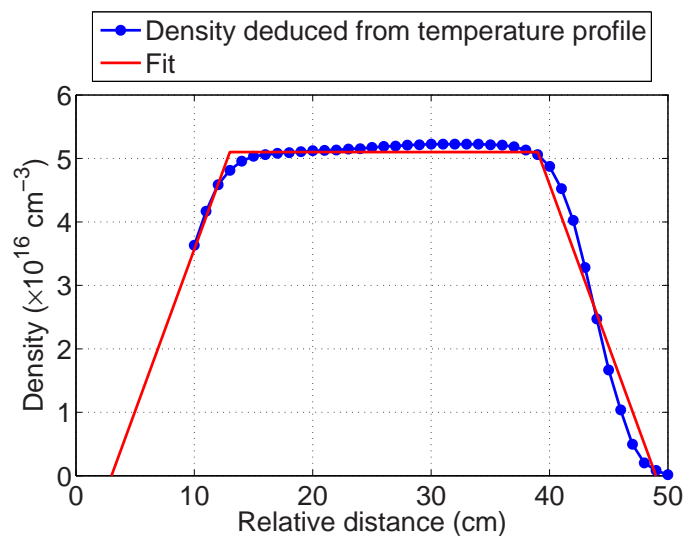
Extended Data Figure 1 | FACET experimental area schematic. Electron beam line features: **a**, beam notching device, **b**, transverse deflecting structure, **c**, initial spectrometer, **d**, final-focus quadrupole magnets, **e**, lithium plasma ionization laser, **f**, lithium vapour column, **g**, spectrometer imaging quadrupole

magnets, **h**, spectrometer dipole magnet, and **i**, Cherenkov and phosphor screens. Bend dipole magnets in the 'W'-shaped chicane are each labelled 'D'. The arrow beneath the e^- symbol indicates the electron beam's direction of motion (left to right).

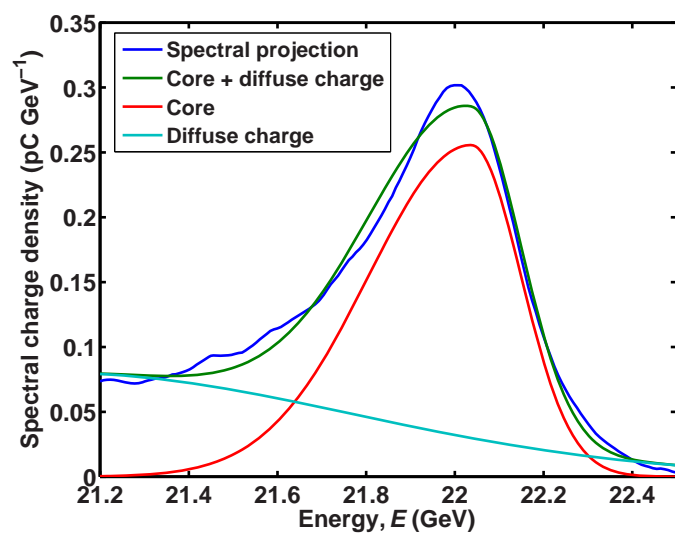


Extended Data Figure 2 | Measured longitudinal profile of two-bunch beam. Image of a typical two-bunch beam streaked onto a profile monitor screen by the transverse deflecting radio-frequency structure (Extended Data Fig. 1b). The drive bunch appears on the right-hand side. Overlaid on the image is the projected longitudinal profile (red line). The left (x) and top (y) axes show the transverse dimensions of the streaked beam on the profile

monitor screen, while the colour axis indicates the charge density of the transverse profile. The bottom (z) axis shows the streaked dimension (y) with the appropriate scaling factor applied to give the corresponding longitudinal coordinate. The right axis shows the linear charge density corresponding to the projected longitudinal profile.



Extended Data Figure 3 | Lithium vapour column density profile. The profile of the neutral vapour pressure density of the lithium vapour column deduced from the measured temperature profile (temperature versus relative distance of insertion of a thermocouple probe) along the heat pipe oven is shown as the blue line. The simple fit used to describe the density profile in our model is shown as the red line.



Extended Data Figure 4 | Fit to accelerated charge. The blue line is the spectral projection of the same data shot shown in Fig. 2c and d. The green line is a fit to the data using a half-Gaussian tail (cyan line) to account for the diffuse, high-angular-divergence accelerated charge plus a full, asymmetric Gaussian (red) used to describe the core of the accelerated trailing bunch after subtracting the half-Gaussian tail.